Soil Moisture Sensing through Phase Measurements in Analog Backscatter Systems

Vincenzo Gentile*
University of Palermo, Italy

Domenico Giustiniano
IMDEA Networks Institute, Spain

Dayrene Frometa
IMDEA Networks Institute, Spain

***Abstract*—Conventional low-cost soil moisture sensors consume milliwatts of power, limiting their scalability for battery-free agricultural IoT. To bridge this gap, we propose a narrowband phase-difference approach for soil moisture estimation using ultra-low-power analog backscatter at 868 MHz. We develop a geometric electromagnetic model relating spatial phase shifts to soil permittivity, proving differential phase remains a valid observable despite refraction across the layered soil–air interface. We further characterize non-ideal hardware effects, establishing how antenna impedance mismatches and other impairments introduce systematic phase biases that require calibration. Our experiments demonstrate reliable discrimination between dry and wet soils, validating a battery-free sensing architecture that offers a scalable solution for sustainable water management.**

I. Introduction

Monitoring soil moisture is a cornerstone of precision agriculture, as water availability directly influences crop health, yield, and resource efficiency. Crucially, the Food and Agriculture Organization (FAO) of the United Nations reports that agriculture consumes nearly 70% of global freshwater resources to irrigate approximately 25% of the world's arable land [1], [2]. These figures underscore the need for accurate and scalable sensing technologies capable of supporting sustainable water management.

Traditional high-precision techniques such as Time Domain Reflectometry (TDR) and Ground Penetrating Radar (GPR) provide reliable estimates of soil water content [3]. However, despite their accuracy, these active systems are expensive and typically operate in the multi-Watt regime, making them fundamentally difficult to scale for monitoring across large agricultural fields.

To reduce the cost of moisture sensing solutions, research has focused on leveraging low-cost wireless technologies to infer soil moisture through radio-frequency (RF) propagation effects. Specifically, electromagnetic propagation through soil is highly sensitive to water content, enabling remote and non-invasive estimation of soil permittivity. To this end, active wireless sensing solutions based on commodity chipsets have been proposed in the literature [4]. However, all active architectures require underground nodes to periodically transmit RF signals, resulting in energy consumption incompatible with long-term deployments.

To address these limitations, battery-free nodes can be leveraged to enable scalable deployments at low maintenance costs. These nodes typically operate on harvested power in the *microwatt* regime and use RF backscatter for communication. In RF backscatter systems, the device reflects an external RF carrier rather than generating its own. The most common operation is *digital backscatter*, which consists of modulating information using discrete signal levels. However, interfacing conventional soil moisture sensors (such as resistive or capacitive probes) requires *milliwatts* of power for active sensing circuitry, making this standard digital approach fundamentally unsuitable for microwatt platforms.

An alternative to digital backscatter communication is *analog backscatter*, where continuous physical variation (such as a sensing voltage or a shifting dielectric load) is mapped directly onto the antenna's impedance. This means that any continuous change in the physical medium translates directly into a proportional shift in the fundamental properties (amplitude, phase, or frequency) of the backscattered wave [5].

Building on this principle, we propose a low-cost narrowband RF sensing method based on *phase-difference measurements* between spatially separated receivers, enabling operation with analog backscatter systems. Because soil permittivity directly affects the RF propagation velocity, we show that the spatial phase difference between two coherent receivers can serve as a highly effective, low-cost observable for estimating soil water content in battery-free systems. We make the following key contributions:

1. Interferometric phase-difference model for soil sensing: We develop a narrowband phase-difference model that captures RF propagation through the layered soil–air medium and the resulting measurement geometry. It shows that the measured phase is a valid observable of soil permittivity despite refraction at the soil–air interface, enabling moisture inference without wideband or time-of-flight measurements.

2. Analysis of non-ideal hardware effects in backscatter: We provide an in-depth analysis of how antenna limitations affect phase accuracy. We show that because physical antennas never perfectly absorb signals, a residual reflection is present. This residual reflection biases the measurement away from the intended geometric value. This results in a hardware offset determined by the specific antenna's properties.

3. Study of two complementary RF architectures: We implement both an active continuous-wave system and a passive analog backscatter system. The active system allows for precise phase control, while the passive system operates battery-free by modulating its internal impedance. We evaluate both in controlled environments to separate hardware-specific offsets from actual soil propagation effects.

4. Experimental evaluation in two soil deployments: We validate the proposed approach in two real soil deployments

with a buried antenna. Across both deployments and architectures, we consistently observe a clear and repeatable phase separation between dry and wet soil conditions, demonstrating battery-free soil moisture discrimination.

II. Background and Related Work

RF propagation in soil is governed by the dielectric properties of the medium, which vary strongly with *volumetric water content* θ_v. This section first introduces the electromagnetic principles that determine how soil permittivity affects phase and time-of-flight (ToF), and then reviews prior RF-based soil moisture sensing systems that exploit these dependencies.

A. Electromagnetic Propagation and Soil Permittivity

In free space, electromagnetic waves propagate at the speed [6]

$$c = \frac{1}{\sqrt{\mu_0 \varepsilon_0}} \approx 3 \times 10^8 \text{ m/s}, \tag{1}$$

where μ_0 and ε_0 denote the magnetic permeability and electric permittivity of free space, respectively. The plane-wave representation of the electric field can be written as

$$\mathbf{E}(\mathbf{r}, t) = \Re\{\mathbf{E}_0 \exp[j(\mathbf{k}\cdot\mathbf{r} - \omega t)]\}, \tag{2}$$

where $\mathbf{E}_0$ is a constant complex amplitude, $\omega = 2\pi f$ is the angular frequency, and $\mathbf{k}$ is the wave vector with magnitude

$$k = \|\mathbf{k}\| = \frac{\omega}{c}. \tag{3}$$

The free-space wavelength is equal to [7]

$$\lambda_0 = \frac{c}{f}. \tag{4}$$

When the wave propagates in a material medium with permittivity ε and permeability μ, the *phase velocity* becomes

$$v_p = \frac{1}{\sqrt{\mu\varepsilon}}. \tag{5}$$

For most non-magnetic materials at radio frequencies, $\mu_r \approx 1$. Therefore, v_p depends mainly on the relative permittivity $\varepsilon_r = \varepsilon/\varepsilon_0$. The wavelength in the medium is then

$$\lambda = \frac{v_p}{f} = \frac{1}{\sqrt{\varepsilon\mu}} \cdot \frac{\lambda_0}{c} = \frac{\lambda_0}{\sqrt{\varepsilon_r \mu_r}} \approx \frac{\lambda_0}{\sqrt{\varepsilon_r}}. \tag{6}$$

The primary parameter of interest in agricultural sensing is the volumetric water content θ_v, defined as the ratio of the volume of liquid water to the total volume of the soil (i.e., $\theta_v = V_w/V_{total}$). The Topp model [8] provides a robust mapping between ε_r and θ_v for mineral soils

$$\varepsilon_r = 3.03 + 9.3\theta_v + 146\theta_v^2 - 76.7\theta_v^3. \tag{7}$$

While deviations of a few percent may occur in highly clay-rich, saline or organic soils [9], the model offers a robust baseline for phase-based permittivity estimation. Regardless of the specific model, a higher θ_v implies a higher ε_r.

B. Phase and Time-of-Flight as Sensing Observables

From Eq. (3), we have that, for a narrowband signal of frequency f, the wave number in soil is

$$k = \frac{2\pi f}{c}\sqrt{\varepsilon_r}, \tag{8}$$

and the accumulated phase shift along a path of length d_p is

$$\Phi(d_p) = -k d_p = -\frac{2\pi f}{c}\sqrt{\varepsilon_r}\, d_p. \tag{9}$$

Correspondingly, the propagation delay, i.e., the *time-of-flight (ToF)*, is

$$\tau = \frac{d_p}{v_p} = \frac{d_p}{c}\sqrt{\varepsilon_r}, \tag{10}$$

which increases with soil moisture. Thus, increasing ε_r increases both the ToF in Eq. (10) and the *magnitude* of the phase accumulation $|\Phi(d_p)|$ in Eq. (9). Since liquid water exhibits $\varepsilon_r \approx 80$, highly saturated soils can reach permittivities of 20–40 [10]. Because of the large dielectric contrast with respect to dry soil ($\varepsilon_r \approx$ 2–3), even small to moderate moisture variations induce detectable RF phase changes.

Phase and ToF thus provide complementary ways to estimate permittivity:

Phase-based sensing: by measuring phase changes $\Delta\Phi$, one can detect variations in ε_r with narrowband signals, but this requires accurate phase values.

ToF-based sensing: by measuring the absolute ToF τ defined in Eq. (10), one obtains a direct propagation delay that avoids phase ambiguity. In practice, wideband systems estimate this τ by leveraging subcarrier-level Channel State Information (CSI) to compute the phase difference ($\Delta\Phi_f$) across multiple subcarriers (Δf), governed by the measurement relation $\tau = -\frac{1}{2\pi}\frac{\boldsymbol{\Delta\Phi_f}}{\Delta f}$. However, extracting this absolute measurement demands complex filtering algorithms to overcome packet detection delay [14].

Relative ToF-based sensing: to bypass the need for strictly synchronized clocks, systems can measure the relative ToF ($\Delta\tau = \tau_1 - \tau_2$) between two receiver antennas. While this relative measurement cancels out the shared hardware delay, reliably extracting the phase-frequency slopes against noise requires wide bandwidth and high-rate processing [15].

C. RF-Based Soil Moisture Sensing: Prior Systems

The above physical dependencies underpin a wide range of active and passive RF sensing systems.

a) Active systems: STROBE [4] uses WiFi MIMO receivers to extract the *relative ToF* $\Delta\tau$ between buried antennas. LoRa-based dual-path sensing [11] alternates two underground antennas using an RF switch and computes phase differences at chirp level. This demands careful phase extraction under narrowband constraints and non-deterministic timing. ZigBee and NB-IoT solutions require underground battery-powered radios [16]–[19].

Table I: Comparison of RF-based Soil Moisture Sensing Systems

System	BW	Frequency	Tx Antennas	Rx Antennas	Accuracy	Phase / ToF Limitations	Constraints
STROBE (WiFi) [4]	70 MHz	2.4 GHz	1 (air)	3 (soil)	∼3%	Rel. ToF only; phase wrapping	Battery-powered (Watt); limited range
LoRa Dual-Antenna [11]	125 kHz	915 MHz	2 (soil)	1 (air)	3.1% avg.	CFO sensitivity; narrowband phase	Active radio (milliwatts); non-synchronous link
RFID GreenTag [12]	26 MHz	902–928 MHz	1 (air)	2 (soil)	<5% (90th perc.)	Power-based (DMRT); no phase	Short range; expensive readers; microwatt tag
Radar Backscatter [13]	>1 GHz	3 GHz	1 (soil)	1 (air)	1.4% avg.	Requires GHz ToF resolution	Battery-assisted tag (340 μW); wideband radar
This Work	**500 KHz**	**868 MHz**	**1 (soil)**	**2 (air)**	**Moisture discrimination validated**	**Hardware bias calibration required**	**μW oscillator-dependent tag; Sensitive to phase errors;**

b) Passive backscatter systems: By reflecting and modulating an incident RF signal, backscatter eliminates the need for power-intensive transmit circuitry. GreenTag [12] places two low-cost passive RFID tags per pot and infers moisture using the Differential Minimum Response Threshold (DMRT), which measures the difference in the *minimum transmission power levels* required to activate each tag. Its scalability is constrained by short communication ranges and the reliance on costly, power-hungry RFID readers. UWB backscatter radar tags [13] estimate moisture from high-resolution ToF measurements, requiring multi-GHz bandwidth that spans portions of licensed spectrum, making it susceptible to interference from, e.g., nearby cellular base stations.

D. Positioning of This Work

A high-level comparison with the proposed methods in the literature is presented in Table I. In contrast to prior work, our system introduced in this work uses a narrowband (500 kHz), sub-GHz (868 MHz) excitation and extracts soil-dependent information solely from the *phase difference* between two coherent receivers.

This architecture: (i) penetrates soil more effectively than 2.4 GHz WiFi, (ii) avoids the high bandwidth of radar systems, (iii) requires no timing synchronization, and (iv) enables battery-free sensing in the microwatt regime.

III. Narrowband RF Phase Difference Model

This section develops the theoretical foundations of the proposed phase-based sensing approach.

A. Signal Model

Let f_c denote the carrier frequency. Following standard time-domain signal processing conventions, the transmitted carrier is modeled as $\cos(\omega_c t)$, where $\omega_c = 2\pi f_c$. Because the receiving antennas convert the incident physical electric field $\mathbf{E}(\mathbf{r}, t)$ into an induced voltage, the time-domain signal processed by the receiver directly inherits the spatial properties of the propagating wave. Specifically, as the wave travels a distance d_p, it accumulates a spatial phase shift $\Phi = -kd_p$.

The backscatter tag modulates and reflects the incident carrier f_c by switching its load impedance according to a waveform $m(t)$ with fundamental frequency f_m.

The backscattered signal can then be written as

$$s_{\text{back}}(t) = A_b m(t) \cos(2\pi f_c t + \Phi), \tag{11}$$

where A_b is the backscattered amplitude and Φ is the accumulated propagation phase. Since $m(t)$ is periodic, the spectrum of $s_{\text{back}}(t)$ contains components at

$$f_c \pm n f_m, \qquad n \in \mathbb{Z}. \tag{12}$$

At the receiver, quadrature demodulation mixes the signal with two orthogonal local oscillator components tuned to $f_{\text{LO}} = f_c$. After low-pass filtering to remove the double-frequency ($2f_c$) components, the resulting In-Phase (I) and Quadrature (Q) baseband signals are

$$I(t) = \frac{A_b}{2} m(t) \cos\Phi, \qquad Q(t) = \frac{A_b}{2} m(t) \sin\Phi. \tag{13}$$

These baseband components preserve the modulation waveform, containing harmonics at multiples of f_m.

B. I/Q Representation of RF Signals

For each antenna, the received complex baseband signal is characterized by the $I(t)$ and $Q(t)$ components derived in Eq. (13), producing the instantaneous phase

$$\phi(t) = \arctan\big(Q(t)/I(t)\big), \tag{14}$$

which enables estimation of channel-induced phase shifts between coherent receivers.

Small (but measurable) phase differences convey information about propagation media, including dielectric variations due to soil moisture.

C. Phase Unwrapping and Synchronization

The $\arctan$ operation in Eq. (14) produces a wrapped phase $\phi_w(t) \in (-\pi, \pi]$, i.e.,

$$\phi(t) = \phi_w(t) + 2\pi k(t), \quad k(t) \in \mathbb{Z}. \tag{15}$$

Sampling the phase at times $t = nT_s$ yields the discrete sequence $\phi_w[n] = \phi_w(nT_s)$.

Let $\Delta\phi_w[n] = \phi_w[n] - \phi_w[n-1]$ denote the discrete wrapped phase increment. If the sampling period T_s is sufficiently small such that the true phase change between consecutive samples satisfies Itoh's criterion $|\phi[n] - \phi[n-1]| < \pi$ [20], the unwrapped increment can be recovered as

$$\Delta\phi_u[n] = \Delta\phi_w[n] - 2\pi\,\text{round}\big(\Delta\phi_w[n]/2\pi\big). \tag{16}$$

Unwrapping may fail under rapid phase changes, low signal-to-noise ratio (SNR), or outliers; in practice, filtering and limiting abrupt jumps improves robustness.

Finally, in coherent dual-receiver setups, the observable is the *spatial phase difference*

$$\Delta\Phi_{12}[n] = \phi_{u,1}[n] - \phi_{u,2}[n] + 2\pi m, \qquad m \in \mathbb{Z}. \quad (17)$$

D. Single-Medium Geometric Phase Model

Having established how the discrete spatial phase difference $\Delta\Phi_{12}$ is extracted and unwrapped, we first relate this observable to the dielectric properties of a single, homogeneous medium. By substituting $\lambda_0 = c/f$ into the propagation model from Eq. (9), and denoting d_{RX1} and d_{RX2} as the effective propagation distances to each receiver, the spatial phase difference becomes

$$\Delta\Phi_{12} = -k(d_{RX1} - d_{RX2}) = \frac{2\pi}{\lambda_0}\sqrt{\varepsilon_r}\,(d_{RX2} - d_{RX1}). \quad (18)$$

Since higher θ_v implies a higher ε_r, the magnitude of the phase accumulation along the propagation path increases, thereby magnifying the absolute measured $|\Delta\Phi_{12}|$.

Eq. (18) highlights the dependence of $\Delta\Phi_{12}$ on soil permittivity. However, estimating ε_r requires knowledge of the relative ToF $\Delta\tau$ to resolve the physical path difference $(d_{RX1} - d_{RX2})$. In narrowband receivers, $\Delta\tau$ cannot be retrieved from phase measurements alone, as no per-subcarrier CSI is available (cf. Section II-B).

Therefore, Eq. (18) cannot be used directly for permittivity estimation, and a formulation that removes this dependence on $(d_{RX1} - d_{RX2})$ is required.

E. Final Phase-to-Permittivity Relation

This section derives a closed-form expression that accounts for refraction geometry across the layered soil-air interface, yielding a direct relation between the measurable phase difference $\Delta\Phi_{12}$ and the soil volumetric water content θ_v.

Let us refer to Fig. 1. The received antennas are separated by d, where

$$d = d_1 + d_2, \quad (19)$$

and

- d_1 is the projected path within soil (transmitter to interface),
- d_2 is the projected path within air (interface to receiver).

Let L_{s1} denote the transmitter burial depth and L_{a1} the receiver height above soil. The geometric projections yield

$$d_1 = L_{s1}\tan\theta_i, \qquad d_2 = L_{a1}\tan\theta_r, \quad (20)$$

so that

$$d = L_{s1}\tan\theta_i + L_{a1}\tan\theta_r. \quad (21)$$

The optical path difference can be decomposed as:

$$\Delta l_1 = d_1\sin\theta_i, \qquad \Delta l_2 = d_2\sin\theta_r,$$

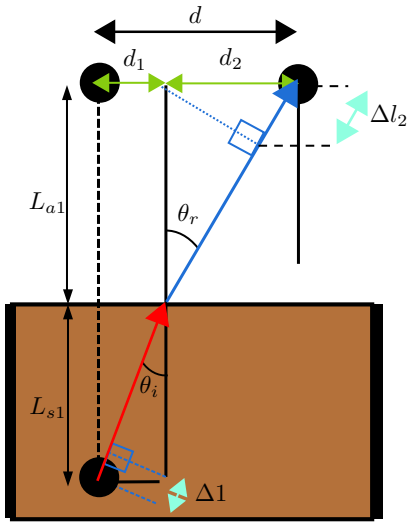

Figure 1: Geometric model of the Tx–Rx configuration.

and the total difference in delay between the two antennas is

$$\Delta\tau = \frac{n\,\Delta l_1}{c} + \frac{\Delta l_2}{c}, \qquad n = \sqrt{\varepsilon_r}.$$

Applying Snell's law $n\sin\theta_i = \sin\theta_r$ eliminates n, yielding

$$n\Delta l_1 = nd_1\sin\theta_i = d_1\sin\theta_r,$$

and therefore

$$\Delta\tau = \frac{(d_1 + d_2)\sin\theta_r}{c} = \frac{d\,\sin\theta_r}{c}.$$

This provides the measurable phase difference

$$\Delta\Phi_{12} = 2\pi f\,\Delta\tau = \frac{2\pi d\,\sin\theta_r}{\lambda}, \quad (22)$$

from which the refraction angle follows as

$$\theta_r = \arcsin\left(\frac{\lambda\Delta\Phi_{12}}{2\pi d}\right). \quad (23)$$

Hence, the measured phase $\Delta\Phi_{12}$ allows estimation of θ_r. Finally, Snell's law [21] provides the soil relative permittivity:

$$\varepsilon_r = \left(\frac{\sin\theta_r}{\sin\theta_i}\right)^2. \quad (24)$$

The estimation of θ_i is performed as follows (cf. Fig. 1). First, the lateral position of the buried transmitting antenna is determined experimentally. Ideally, this is achieved by hovering the receiver array above the soil surface and translating it laterally until the spatial phase difference $\Delta\Phi_{12}$ between RX1 and RX2 becomes zero. This condition indicates that the propagation paths from the transmitter to both receiver antennas are perfectly symmetric. However, as we will detail in Section IV and prove in the experimental evaluation in Section VI, real-world measurements introduce a systematic bias. Therefore, in practice, the receiver is aligned directly above the buried transmitter when the measured phase difference $\Delta\Phi_{12}$ converges to this pre-calibrated baseline offset, rather than absolute zero.

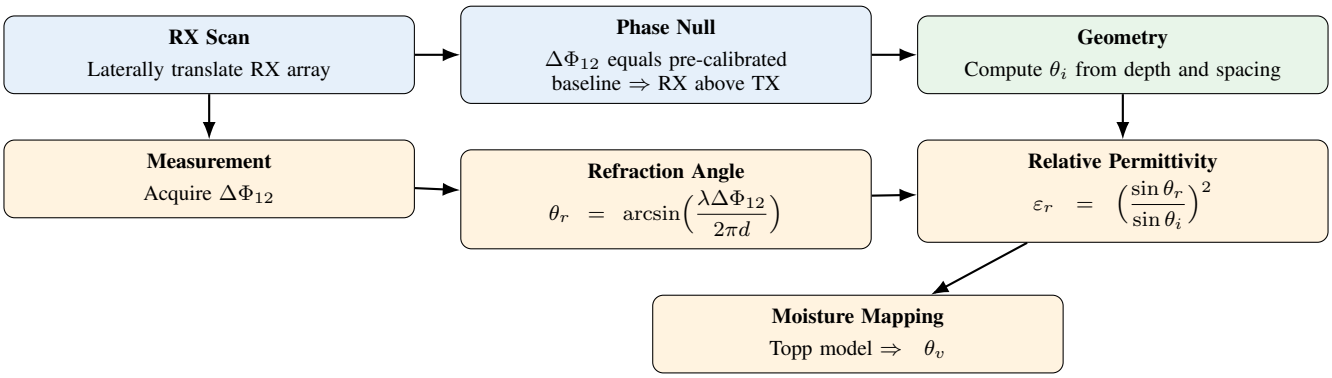

Figure 2: Phase-to-permittivity and moisture estimation.

Once the transmitter position is known, the incidence angle θ_i is computed from the fixed antenna separation and burial depth using $d_1 = L_{s1} \tan\theta_i$ defined in Eq. (20). Substituting the resulting ε_r into the Topp model (cf. Section II-A) enables a direct mapping from the measured $\Delta\Phi_{12}$ to the volumetric water content θ_v. A high-level summary of all steps of the proposed estimator is presented in Fig 2.

Discussion. The above derivation formally establishes that the differential-phase quantity $\Delta\Phi_{12}$ behaves as an interferometric observable in the presence of layered soil–air propagation. Importantly, the estimator does not require access to the relative ToF between two antennas, but depends only on the *geometric imbalance* between the two receiving paths. This demonstrates that classical phase-difference interferometry remains valid in this scenario: the phase observable retains its dependence on the refracted angle θ_r, and thus on ε_r, *even though the propagation is not purely geometric-line-of-sight*.

IV. Hardware-Induced Phase

While the previous sections relate the measured phase difference to the propagation geometry and soil permittivity, the analysis implicitly assumes ideal impedance conditions at the battery-free tag antenna. In practice, however, the antenna impedance may deviate from the nominal design value. These impedance mismatches introduce additional phase shifts in the backscattered signal that are unrelated to propagation effects. In this section we analyze how these non-idealities translate into residual phase offsets in the measured baseband signal.

The reflection coefficient of the tag is defined as

$$\Gamma = \frac{Z_L - Z_{ant}}{Z_L + Z_{ant}}, \tag{25}$$

where Z_L denotes the load impedance and Z_{ant} the antenna input impedance.

The battery-free tag alternates between two impedance states yielding On-Off Keying (OOK) modulation:

- **Reflecting state:** the antenna port is short-circuited ($Z_L = 0\,\Omega$), producing $\Gamma_R = -1$ and therefore full reflection of the incident signal.

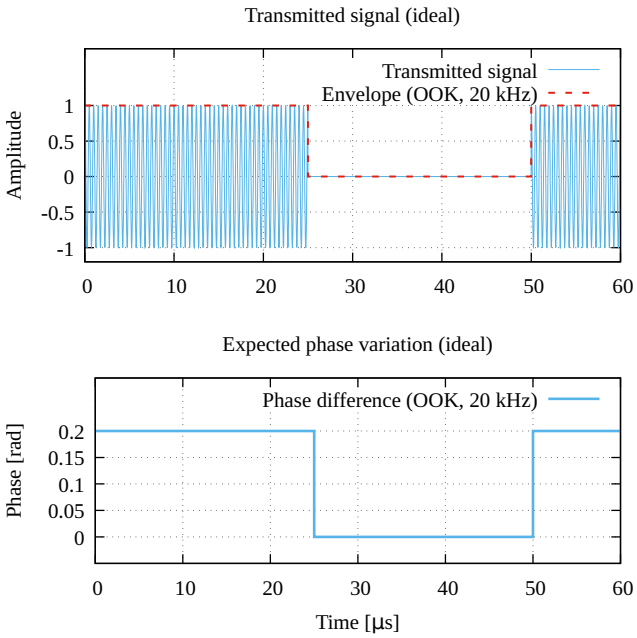

Figure 3: Ideal backscattered signal and phase variations, assuming perfect impedance matching in the absorbing state ($\Gamma_A = 0$) and a spatial differential phase of $\Delta\Phi_{12} = 0.2$ rad.

- **Absorbing state:** the antenna is terminated with a $Z_L = 50\,\Omega$ load, yielding $\Gamma_A = 0$ and full power transfer to the load.

Figure 3 illustrates the ideal reference scenario of a battery-free tag, where the antenna alternates between perfectly matched and fully reflective states. The transmitted amplitude therefore follows an ideal square-wave envelope, and the measured phase variation is strictly synchronized with the ON (reflecting)/OFF (absorbing) timing.

However, we observe residual phase rotation in real implementations due to the *non-ideal impedance of the tag antenna* with respect to the ideal $Z_{ant} = 50\,\Omega$ reference. In fact, because analog backscatter relies on controlled impedance switching, any deviation of the antenna impedance from the nominal design value alters the complex reflection coefficient

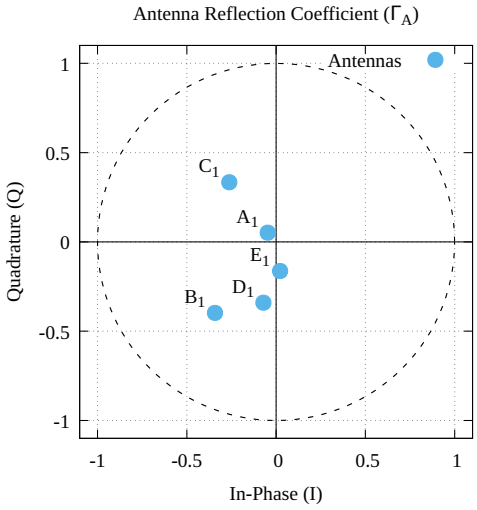

Figure 4: IQ-plane representation of the antenna reflection coefficients Γ_A during absorption state at 868 MHz for five antenna models (A_1–E_1) based on experimental measurements. The dashed unit circle denotes $|\Gamma| = 1$. Differences in antenna impedance introduce distinct phase rotations in the backscattered signal.

Γ at the antenna–tag interface.

Formally, in the non-ideal case, the complex reflection coefficient $\Gamma(t)$ can be expressed in polar form as $|\Gamma(t)|e^{j\phi_\Gamma(t)}$. The real-valued backscattered signal can then be modeled as

$$s_{\text{back}}(t) = A_b\,|\Gamma(t)|\cos(2\pi f_c t + \Phi + \phi_\Gamma(t)), \tag{26}$$

where the magnitude $|\Gamma(t)|$ and phase $\phi_\Gamma(t)$ alternate between two values associated with the "ON" and "OFF" load states (e.g., $\phi_\Gamma = \pi$ for an ideal reflection). Unlike the ideal model of Eq. (14), this formulation explicitly captures the hardware-induced phase variations introduced by antenna mismatch.

To quantitatively assess this variability, we measure the complex input impedance of five antennas at 868 MHz using a high-end Rohde & Schwarz ZNLE18 vector network analyzer. The measured impedances are reported in Table II. Despite similar nominal frequency ratings, the antennas exhibit substantial differences in both resistive and reactive components, spanning inductive and capacitive regimes.

Fig. 4 visualizes this effect by plotting the complex reflection coefficients Γ at 868 MHz of these five representative sub-GHz antennas in the IQ plane (including A_1, used for the experiments in this work). The dashed unit circle highlights the magnitude of Γ, while the angular separation between points emphasizes the antenna-dependent phase contribution. Although all antennas operate in the same frequency band,

Table II: VNA-measured antenna impedances at 868 MHz.

ID	Model (Manufacturer)	Impedance @ 868 MHz
A_1	ANT-8WHIP3H-SMA (Pulse)	$54.6 - j5.7\ \Omega$
B_1	1001826 (KYOCERA)	$61.4 + j67.3\ \Omega$
C_1	2125700150 (Molex)	$62.5 - j50.9\ \Omega$
D_1	RFPCA791010IMRB301 (Walsin)	$44.9 + j34.8\ \Omega$
E_1	Generic (N/A)	$45.4 + j15.2\ \Omega$

their reflection coefficients exhibit significantly different IQ rotations. As a result, the phase measurement is subject to a bias when the OFF state is not perfectly absorbing.

On the other hand, under the ideal short-circuit assumption used for the reflecting state, $\Gamma_R = -1$ independently of the antenna impedance. Therefore, unlike the absorbing state, the reflecting state does not introduce antenna-dependent variation in the IQ plane in this simplified model, although small deviations may arise due to non-ideal switching circuitry.

Impact on measurements. After coherent downconversion and low-pass filtering, the signal in Eq. (26) is mapped to the complex baseband. Letting Φ_i represent the total phase measured at receiver i during the "ON" state (combining the spatial propagation phase and the tag's ON-state hardware phase), the complex vectors during the "ON" ($\vec{V}_{\text{on},i}$) and "OFF" ($\vec{V}_{\text{off},i}$) states can be expressed as:

$$\vec{V}_{\text{on},i} = A_{\text{on},i}e^{j\Phi_i}, \qquad \vec{V}_{\text{off},i} = A_{\text{off},i}e^{j\Phi_{\text{off},i}}, \tag{27}$$

where $A_{\text{on},i}$ and $A_{\text{off},i}$ denote the amplitudes of the reflected and residual absorbing-state signals, respectively, and $\Phi_{\text{off},i}$ represents the phase of the residual OFF-state vector.

To eliminate the static carrier leakage from the transmitter, the DC component of the received baseband signal is removed. The soil moisture sensing system then computes the average phase offset at each receiver i, which can be defined as the angle of the complex vector sum:

$$\hat{\Phi}_i = \angle(\vec{V}_{\text{on},i} + \vec{V}_{\text{off},i}) = \Phi_i + \delta_i, \tag{28}$$

where δ_i represents the hardware-induced phase bias.

Finally, the differential phase measured between the two antennas at the receiver is

$$\widehat{\Delta\Phi}_{12} = (\hat{\Phi}_1 - \hat{\Phi}_2) + \Delta\Phi_{\text{RX}} = \Delta\Phi_{12} + \delta_{\text{tag}} + \Delta\Phi_{\text{RX}}, \tag{29}$$

where $\Delta\Phi_{12} = (\Phi_1 - \Phi_2)$ represents the true spatial phase difference defined in Eq. (17), $\delta_{\text{tag}} = (\delta_1 - \delta_2)$ is the tag baseline offset due to its non non-idealities and $\Delta\Phi_{\text{RX}}$ represents any internal phase imbalance between the receiver's RF chains (such as cable length mismatches).

In the ideal case ($\Gamma_A = 0$), averaging in Eq. (28) does not affect the measured phase, as the OFF state contributes no energy to the vector sum, leaving the geometric phase Φ_i perfectly preserved. On the other hand, a real antenna mismatch results in a residual vector $\vec{V}_{\text{off},i}$ that induces an angular deviation, δ_i, relative to the ideal geometric phase.

For instance, as shown in Fig. 5, if $\vec{V}_{\text{off}}$ is oriented at $65°$ with a magnitude of $A_{\text{off}} = 0.4$, a signal with an initial propagation phase of $\Phi_1 = 0°$ experiences a phase shift of $\delta_1 \approx 19.5°$. However, if the propagation phase shifts to $\Phi_2 = 35°$, the same static hardware vector results in a reduced angular deviation of $\delta_2 \approx 11°$. This disparity ($\delta_1 \neq \delta_2$) demonstrates that the hardware bias δ_{tag} is a nonlinear function of the propagation angle.

Crucially, the tag's reflection coefficients are not static. When the tag is deployed underground, the soil acts as a *dielectric load* that physically couples with the antenna. This

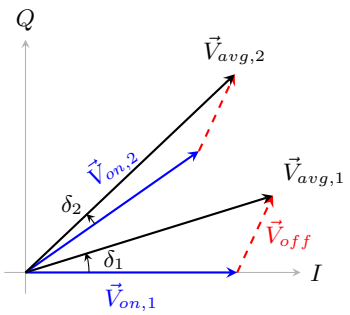

Figure 5: Non-linear phase bias for the A_1 antenna configuration. The fixed hardware-induced vector $\vec{V}_{off}$ biases the geometric signal $\vec{V}_{on}$ differently at each receiver, resulting in an angle-dependent phase bias ($\delta_1 \neq \delta_2$).

loading fundamentally alters the antenna's complex input impedance as a function of the soil's permittivity (water content) [22]. Consequently, the residual vector $\vec{V}_{\text{off}}$ and the resulting tag bias δ_{tag} become highly dynamic parameters directly driven by soil moisture.

Consequently, to accurately recover the underlying soil-induced phase shifts, the measured spatial phase difference $\widehat{\Delta\Phi}_{12}$ must be calibrated against both the static receiver offset ($\Delta\Phi_{\text{RX}}$) and the dynamic hardware bias (δ_{tag}), as will be detailed in the experimental evaluation in Section VI.

V. Experimental Setup

We investigate two RF architectures that exploit phase-difference interferometry for soil moisture sensing. We operate in the sub-GHz ISM band at 868 MHz, motivated by prior underground link-budget analyses showing that soil attenuation increases rapidly with carrier frequency, especially at higher volumetric water content [13]. In detail, we study:

1. An **active continuous-wave (CW) system** using a USRP B210 with a monopole antenna that radiates the field at the carrier frequency with 20 kHz modulation. A block diagram is shown in Fig. 6.

2. A **passive analog backscatter system** in which a battery-free tag modulates and reflects the external CW carrier. The passive architecture replaces local RF generation with a battery-free tag that modulates the externally provided CW. Its impedance-switching network generates backscatter sidebands at $f_c \pm n f_m$, driven by a f_m =20 kHz square wave from an Analog Discovery 2 to facilitate experimental testing. The setup is shown in Fig. 7.

Another B210 performs **coherent reception** using two identical +3 dBi monopole antennas spaced at $\lambda/2$. The receiver employs phase-matched RF chains, including identical antennas and coaxial cables, to ensure high physical symmetry and minimize instrumentation-induced phase biases.

To analyze the full spectral distribution of the backscattered signal at the receiver, we capture data at 1 MSps (Fig. 8). The receiver is tuned to $f_{\text{LO}} = f_c$. As illustrated, the baseband square-wave structure and its most significant harmonics fall within a $\pm$250 kHz region. Therefore, for standard operation, our system acquires samples at 500 kSps. This bandwidth

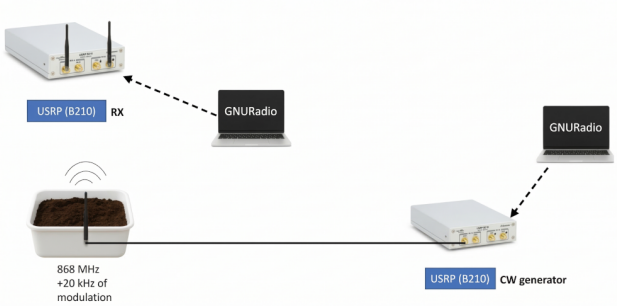

Figure 6: Block diagram of System 1.

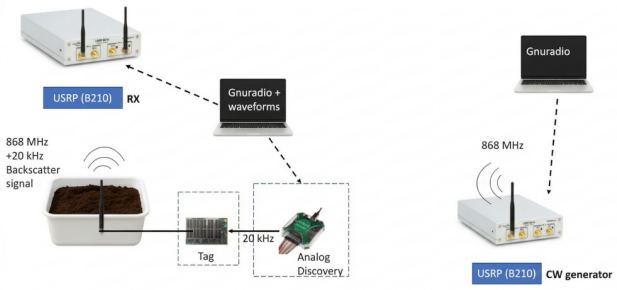

Figure 7: Block diagram of System 2.

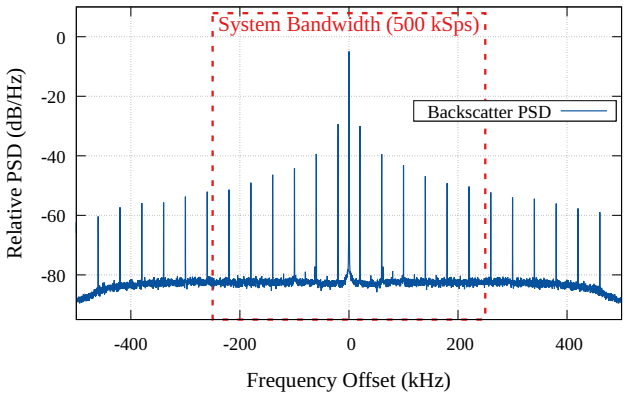

Figure 8: Power spectrum density (PSD) of the received backscatter signal. The prominent 20 kHz harmonics correspond to the analog switching/modulation frequency of the battery-free tag, allowing separation from the carrier.

is sufficient to preserve the crucial 20 kHz modulation harmonics, thereby improving the robustness of phase estimation while minimizing the noise floor.

A. Battery-Free Tag and Soil

A photograph of the tag used in the experiments is shown in Fig. 9. The tag is connected to an ANT-8WHIP3H-SMA antenna, buried 5 cm beneath the soil surface and deployed horizontally to promote *uniform moisture conditions*.

The soil medium used for the experiments is a highly porous organic soil composed primarily of peat and perlite. Approximately 13 liters of this soil are placed in a $25 \times 35 \times 15$ cm container. To achieve *wet soil* conditions, approximately 2 liters of water are added, corresponding to a

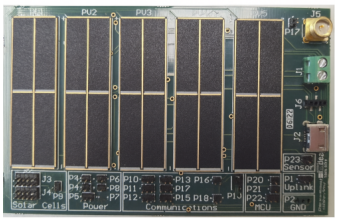

Figure 9: Battery-free IoT backscatter tag used in System 2.

volumetric water content (θ_v) increase of roughly 15.4%, to ensure the soil is completely saturated.

Based on the Topp model in Eq. (7), this moisture level yields a relative permittivity $\varepsilon_r \approx 7.6$. As established in Section II-B, this dielectric shift ensures a strong accumulated phase difference between the dry and wet soil states.

B. Signal Processing Overview

Raw I/Q samples are acquired in GNU Radio and processed in MATLAB. The processing chain performs: (i) removal of DC component, (ii) phase $\phi(t)$ extraction and unwrapping on each received antenna, (iii) alignment to remove 2π ambiguities, and (iv) computation of the spatial phase difference $\Delta\Phi_{12}$. A peak-detection strategy on RX1 is used to enforce a consistent reference, improving stability and repeatability.

We then describe the key system parameters that enable stable and repeatable phase-difference measurements.

1) Frequency Alignment and DC Offset Mitigation: Small DC offsets distort the phase baseline in both systems. The Tag (and System 1 modulation) generates spectral components at $f_c \pm nf_m$. Residual distortion is then mitigated in post-processing using software DC blocking.

2) Magnitude Metric: Signal magnitude is computed as

$$\mathrm{MAG}[n] = \sqrt{I[n]^2 + Q[n]^2},$$

and is monitored to ensure adequate SNR. Across all trials, MAG remains well above noise floor, enabling reliable phase estimation even when soil attenuation reduced absolute received power.

3) Far-Field and Antenna Polarization: The Tx–Rx separation exceeds 2λ to ensure planar-wave conditions. We experimentally observe that using the same polarization between the antennas produces higher MAG in free-space, consistent with theory. Orthogonal polarization was also examined experimentally but produced weaker received magnitude, consistent with polarization mismatch properties. In soil, the contrast between vertical and horizontal reduced, likely due to scattering-induced depolarization. Nevertheless, the same polarization is adopted for all soil measurements to maximize sensitivity and robustness.

4) Geometric Tx–Rx Placement: Three transmitter positions relative to RX1–RX2 are evaluated as shown in Fig. 10: centered, toward RX1, toward RX2: the symmetric case (Configuration 1) with the transmitting antenna aligned to the center of the receiver, while in Configurations 2 and 3 the transmitting antenna moved by $\lambda = 34.8\,\mathrm{cm}$ with respect to the center of the receiver.

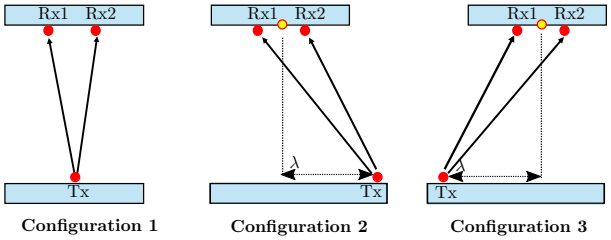

Figure 10: Transmitter placement relative to RX1–RX2 for the three geometries used in the experiments.

VI. Experimental Evaluation

This section reports the experimental evaluation of the proposed phase-difference method for soil moisture sensing. The goals are to: (i) validate the geometric phase-difference model, (ii) assess the impact of soil permittivity under dry and wet conditions, and (iii) evaluate practical effects, such as hardware impairments and short-term behavior.

A. Free-Space Validation

We first validate the system in free space to verify the geometric model without the influence of the soil medium. As discussed in Section III-D, Eq. (18) cannot be used directly for soil permittivity estimation. However, in a controlled over-the-air environment ($\epsilon_r \approx 1$), the propagation distances are strictly determined by the known measurement geometry, allowing us to use this setup to explicitly verify the underlying geometric phase-difference model.

For a transmitter placed at distance h with respect to the receiver line, laterally displaced by a distance Δx from the midpoint between RX1 and RX2 and considering an antenna spacing at the receiver of s, the propagation distances are:

$$d_{RX1} = \sqrt{h^2 + (\Delta x + s/2)^2}, d_{RX2} = \sqrt{h^2 + (\Delta x - s/2)^2}. \tag{30}$$

Setting $\epsilon_r = 1$ in Eq. 18, the path difference $\Delta d = d_{RX2} - d_{RX1}$ results in a theoretical phase shift $\Delta\Phi_{\text{geom}}$ defined by:

$$\Delta\Phi_{\text{geom}} = \frac{2\pi}{\lambda_0}\,\Delta d. \tag{31}$$

Tests are conducted using both System 1 and 2 with distance between TX and receiver of $h = 70\,\mathrm{cm}$. Ten acquisitions are averaged on each measurement to mitigate noise.

In the symmetric Configuration 1 ($\Delta x = 0$, hence $d_{RX1} = d_{RX2}$), the model predicts a null phase difference. We observe that System 1 accounts for a stable system bias ($\Delta\Phi_{\text{RX}} \approx 0.6\,\mathrm{rad}$) in Configuration 1 which is likely due to residual phase imbalances between the receiver's RF chains. System 2 exhibits the same geometric trends after including the Tag offset contribution ($\delta_{\text{tag}} \approx 1.2{-}1.3\,\mathrm{rad}$). This bias remains stable across repeated measurements, confirming that it arises from a fixed hardware-related phase offset (cf. Section IV).

When the transmitter is displaced laterally, the model predicts a nonzero phase difference of opposite sign depending on whether the transmitter is closer to RX1 or RX2. For the experimental geometry considered here, the expected value is $\Delta\Phi_{\text{geom}} \approx \pm 1.26$ rad. The experimental measurements in the

(a) Deployment 1: receiver at soil height.

(b) Deployment 2: elevated receiver, with two tested transmitter configurations.

Figure 11: Experimental deployments using a passive analog backscatter tag, with antenna buried in the soil.

two asymmetric configurations (Configurations 2 and 3) are in good quantitative agreement with this prediction once the intrinsic phase bias $\Delta\Phi_{\mathrm{RX}} \approx 0.60$ rad, estimated from the symmetric case, is taken into account.

Specifically, when the transmitter is closer to RX1, the corrected expected phase difference is $\Delta\Phi_{\mathrm{exp}} \approx 1.86$ rad, which closely matches the average measured value of about $+1.8$ rad, while a displacement towards RX2 yields a corrected expected value of $\Delta\Phi_{\mathrm{exp}} \approx -0.66$ rad, consistent with the measured average of approximately -0.57 rad.

Overall, these results confirm that the observed phase differences in free space are accurately captured by the geometric model, with deviations from the ideal behavior primarily arising from systematic hardware effects rather than from unmodeled propagation phenomena.

B. Soil Measurements - Deployment 1

We present results from two different deployments with the antenna buried in the soil. Figure 11a shows *deployment 1*, with the dual-receiver array positioned at the same height as the soil surface to study near-ground propagation.

1) Dry vs. Wet Traces: Figure 12 shows the spatial phase difference $\widehat{\Delta\Phi}_{12}$ in Configuration 1 (centered) for System 2. The figure illustrates a clear, persistent separation between dry (blue) and wet (green) soil conditions for measurements conducted across different times.

In particular, we observe that the measurements under dry soil cluster around 3.1–3.2 rad. Note that this dry soil baseline differs significantly from the free-space baseline ($\approx 1.8 - 1.9$ rad) observed in Section VI-A. While the geometric setup of Configuration 1 is symmetric ($\Delta x = 0$), burying the tag introduces dielectric loading (cf. Section IV).

Table III: System 1 phase differences under dry and wet soil.

Configuration	Dry	Wet
1 – centered	0.382	0.762
2 – toward RX2	0.743	0.944

Table IV: System 2 phase differences under dry and wet soil.

Configuration	Dry	Wet
1 – centered	3.210	3.410
2 – toward RX2	3.111	3.533

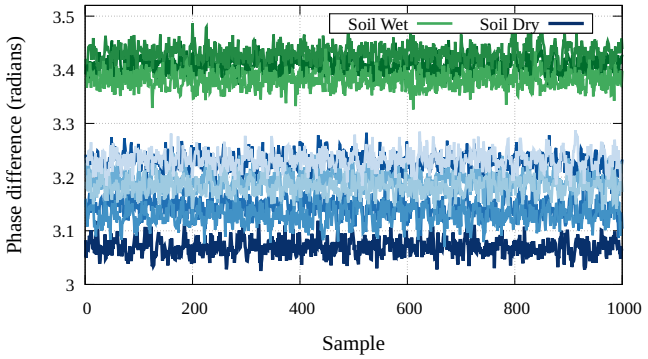

Figure 12: Representative spatial phase difference $\widehat{\Delta\Phi}_{12}$ traces for deployment 1 under dry vs. wet conditions (System 2) with tag antenna buried in the soil.

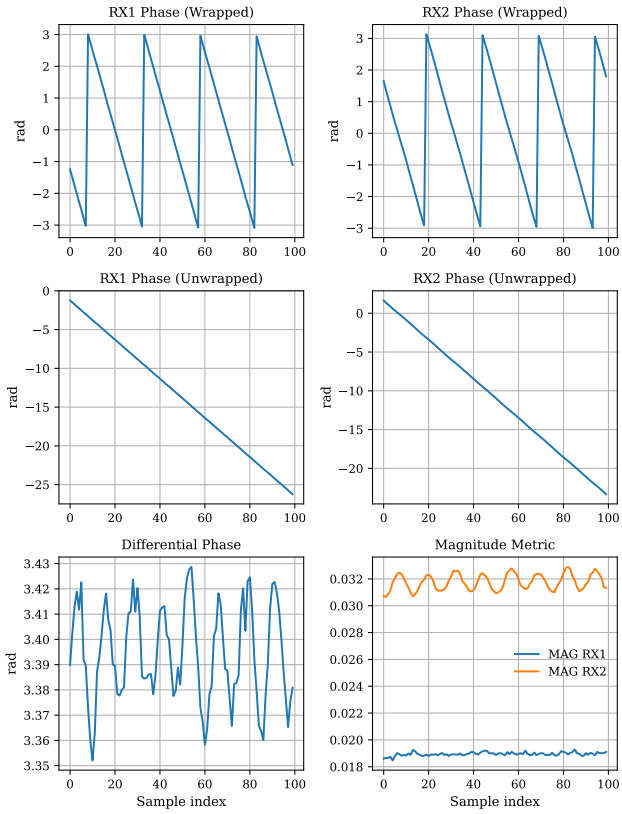

Figure 13: Representative traces in Deployment 2 over the first 100 samples obtained from the passive backscatter system (System 2), with antenna buried in the soil. The top and middle figures show the wrapped and unwrapped phase at RX1 and RX2, respectively. The bottom-left figure reports the resulting differential phase $\widehat{\Delta\Phi}_{12}$, while the bottom-right figure shows the signal magnitude MAG.

Because the antenna's reactive near field interacts directly with the surrounding soil, the effective loading becomes sensitive to the local dielectric environment. This physical coupling breaks the electromagnetic symmetry of the ideal free-space environment, causing the differential hardware bias

(δ_{tag}) to shift the measured baseline.

Building upon this dry baseline, the further systematic phase shift observed under wet conditions (upward to 3.35–3.45 rad) reflects the increase in permittivity caused by water. This elevated permittivity alters the tag's overall reflection coefficient Γ, which in turn modifies the residual vector $\vec{V}_{\text{off}}$. Consequently, the combined effect of soil-dependent hardware loading and permittivity-dependent phase propagation helps discriminate moisture levels even in geometrically centered deployments.

C. Soil Measurements - Deployment 2

In *deployment 2*, the receiver array is elevated at a height of 70 cm from the soil surface, while the transmitter placement inside the soil is varied according to the Configuration 1 and 2 defined in Fig. 10. The deployment is shown in Fig. 11b, including the tag. Experiments in each configuration are repeated under dry and wet conditions for both systems.

1) System 1 (continuous transmission) in soil: Results are reported in Table III. Each entry in the table represents the average over ten acquisitions. Wet soil consistently produces larger absolute phase values than dry soil. This aligns closely with the underlying electromagnetic models in Section III where an increase in soil permittivity drives a proportional increase in the accumulated spatial phase by a factor of $\sqrt{\varepsilon_r}$.

2) System 2 (passive tag) in soil: System 2 shows the same wet–dry trend in Table IV, although the intrinsic Tag offset dominates absolute values.

3) Processing at trace level with passive tag: We study the short-term behavior of the extracted phase and magnitude signals to validate the proposed processing chain. Figure 13 shows representative phase and magnitude trace obtained from System 2 over the first 100 samples. The wrapped phase at each receiver exhibits the expected periodic behavior, while phase unwrapping reveals a common linear trend.

The measured spatial phase difference $\widehat{\Delta\Phi}_{12}$ reported at the bottom left shows fluctuation due to the signal modulation $m(t)$. The figure also reports the signal magnitude ($\text{MAG} = \sqrt{I^2 + Q^2}$), which remains stable over the observation window, indicating stable coupling and sufficient signal-to-noise ratio for reliable phase estimation. These results demonstrate that robust differential phase measurements can be obtained within a short acquisition window, and thus possible with passive tag operating under μW power budget.

VII. Conclusion

This work demonstrated the feasibility of narrowband RF phase-difference interferometry for soil moisture sensing through a combined geometric and electromagnetic model valid under layered propagation. Our experimental deployments confirmed this capability by successfully detecting moderate moisture variations. Currently, challenges such as hardware asymmetries and dielectric load make this method best suited for coarse moisture classification. Nevertheless, its distinct advantages in power consumption and hardware simplicity make it highly attractive for scalable, low-cost agricultural sensing, motivating future work to improve its precision for passive, battery-free applications.

Acknowledgment

This work has been partially funded by TUCAN6-CM (TEC-2024/COM-460), funded by CM (ORDEN 5696/2024). We thank Javier Talavante, Fernando Gonzalez, Edson Dos Santos and Salvatore Corallo for their feedback.

References

[1] Food and Agriculture Organization of the United Nations (FAO), "Water for sustainable food and agriculture," FAO, Rome, Italy, Tech. Rep., 2017, a report produced for the G20 Presidency of Germany.

[2] K. Zhang, X. Li, D. Zheng, L. Zhang, and Z. Gaofeng, "Estimation of global irrigation water use by the integration of multiple satellite observations," *Water Resources Research*, vol. 58, 03 2022.

[3] J. H. et al., "Soil water content measurements at different scales: accuracy of time domain reflectometry and ground-penetrating radar," *Journal of Hydrology*, vol. 245, no. 1, pp. 48–58, 2001.

[4] J. Ding and R. Chandra, "Towards low cost soil sensing using wi-fi," in *The 25th Annual International Conference on Mobile Computing and Networking*, ser. ACM MobiCom '19, 2019.

[5] M. Padmal, D. Piumwardane, D. Giustiniano, T. Voigt *et al.*, "Localization and tracking of ambient rf sources with analog backscatter tags," in *ACM/IEEE International Conference on Modelling, Analysis and Simulation of Wireless and Mobile Systems*, 2025.

[6] D. Fleisch, *A student's guide to Maxwell's equations*. Cambridge University Press, 2008.

[7] C. A. Balanis, *Antenna Theory: Analysis and Design*. Wiley, 2016.

[8] G. C. Topp, J. L. Davis, and A. P. Annan, "Electromagnetic determination of soil water content: Measurements in coaxial transmission lines," *Water Resources Research*, vol. 16, no. 3, pp. 574–582, 1980.

[9] C. Roth, M. Malicki, and R. Plagge, "Empirical evaluation of the relationship between soil dielectric constant and volumetric water content as the basis for calibrating soil moisture measurements by tdr," *Journal of Soil Science*, vol. 43, no. 1, pp. 1–13, 1992.

[10] M. C. e. a. Dobson, "Microwave dielectric behavior of wet soil-part ii: Dielectric mixing models," *IEEE Transactions on Geoscience and Remote Sensing*, vol. GE-23, no. 1, pp. 35–46, 1985.

[11] Z. Chang, F. Zhang, J. Xiong, J. Ma, B. Jin, and D. Zhang, "Sensor-free soil moisture sensing using lora signals," *Proc. ACM Interact. Mob. Wearable Ubiquitous Technol.*, vol. 6, no. 2, Jul. 2022.

[12] J. Wang, L. Chang, S. Aggarwal, O. Abari, and S. Keshav, "Soil moisture sensing with commodity rfid systems," ser. ACM MobiSys '20, 2020, p. 273–285.

[13] C. Josephson, M. Kotaru, K. Winstein, S. Katti, and R. Chandra, "Low-cost in-ground soil moisture sensing with radar backscatter tags," ser. ACM COMPASS '21, 2021, p. 299–311.

[14] M. Rea, A. Fakhreddine, D. Giustiniano, and V. Lenders, "Filtering noisy 802.11 time-of-flight ranging measurements from commoditized wifi radios," *IEEE/ACM Transactions on Networking*, vol. 25, no. 4, pp. 2514–2527, 2017.

[15] M. Kotaru, K. Joshi, D. Bharadia, and S. Katti, "Spotfi: Decimeter level localization using wifi," ser. ACM SIGCOMM '15, 2015, p. 269–282.

[16] H. R. Bogena *et al.*, "Soilnet – a zigbee based soil moisture sensor network," in *AGU Fall Meeting Abstracts*, 2007.

[17] H. R. Bogena, A. Weuthen, and J. A. Huisman, "Recent developments in wireless soil moisture sensing to support scientific research and agricultural management," *Sensors*, vol. 22, no. 24, p. 9792, 2022.

[18] I. Luka, L. Lin, W. Gu *et al.*, "Soil moisture monitoring system based on wireless sensor network," *Advances in Engineering Research*, 2017.

[19] Y. Wu, Z. Yang, and Y. Liu, "Internet-of-things-based multiple-sensor monitoring system for soil information diagnosis using a smartphone," *Micromachines*, vol. 14, no. 7, p. 1395, 2023.

[20] K. Itoh, "Analysis of the phase unwrapping algorithm," *Applied Optics*, vol. 21, no. 14, pp. 2470–2470, 1982.

[21] J. D. Jackson, *Classical Electrodynamics*, 3rd ed. Wiley, 1999.

[22] A. Salam and U. Raza, "Signals in the soil: underground antennas," in *Signals in the Soil: Developments in Internet of Underground Things*. Springer, 2020, pp. 189–215.